Monthly Notices
of the
ROYAL ASTRONOMICAL SOCIETY

Mon. Not. R. Astron. Soc. **418,** 1004–1011 (2011) doi:10.1111/j.1365-2966.2011.19551.x

Numerical simulations of high Lundquist number relativistic magnetic reconnection

O. Zanotti[1]★ and M. Dumbser[2]

[1]*Max-Planck-Institut für Gravitationsphysik, Albert Einstein Institut, D-14476 Golm, Germany*
[2]*Laboratory of Applied Mathematics, University of Trento, Via Mesiano 77, I-38100 Trento, Italy*

Accepted 2011 August 1. Received 2011 July 7; in original form 2011 March 30

ABSTRACT

We present the results of 2D and 3D magnetohydrodynamical numerical simulations of relativistic magnetic reconnection, with particular emphasis on the dynamics of the plasma in a Petschek-type configuration with high Lundquist numbers, $S \sim 10^5$–10^8. The numerical scheme adopted, allowing for unprecedented accuracy for this type of calculations, is based on high-order finite volume and discontinuous Galerkin methods as recently proposed by Dumbser & Zanotti. The possibility of producing high Lorentz factors is discussed, showing that Lorentz factors close to ∼4 can be produced for a plasma parameter $\sigma_{\rm m} = 20$. Moreover, we find that the Sweet–Parker layers are unstable, generating secondary magnetic islands, but only for $S > S_{\rm c} \sim 10^8$, much larger than what is reported in the Newtonian regime. Finally, the effects of a mildly anisotropic Ohm's law are considered in a configuration with a guide magnetic field. Such effects produce only slightly faster reconnection rates and Lorentz factors of about 1 per cent larger with respect to the perfectly isotropic Ohm's law.

Key words: instabilities – magnetic reconnection – MHD – relativistic processes.

1 INTRODUCTION

Relativistic magnetic reconnection is recognized to be a key physical process in high-energy astrophysics, being able to convert magnetic energy into heat and plasma kinetic energy over short timescales. Relevant examples include (i) the magnetospheres of pulsars near the Y-point, where the outermost magnetic field lines intersect the equatorial plane (Uzdensky 2003; Gruzinov 2005); (ii) the dissipation of alternating fields at the termination shock of a relativistic striped pulsar wind (Pétri & Lyubarsky 2007); (ii) soft gamma-ray repeaters, where giant magnetic flares could be the explanation of the observed strongly magnetized and relativistic ejection events (Lyutikov 2003, 2006); (iv) gamma-ray burst jets, where particle acceleration by magnetic reconnection in electron–positron plasmas is supposed to take place (Drenkhahn & Spruit 2002; Barkov & Komissarov 2010; McKinney & Uzdensky 2010; Rezzolla et al. 2011) and (v) accretion disc coronae of active galactic nuclei, where violent releases of energy may be generated by Petschek magnetic reconnection of strong magnetic loops emerging from the disc via buoyancy instability[1] (di Matteo 1998; Schopper, Lesch & Birk 1998; Jaroschek, Lesch & Treumann 2004). Very recently, moreover, Nalewajko et al. (2011) have described a model of minijets in blazars to explain their ultrafast variability and were able to fit data of PKS2155−304 assuming that the dynamics is governed by relativistic magnetic reconnection with a weak 'guide magnetic field', i.e. with a magnetic field aligned to the current.

In the recent past, both theoretical studies and numerical investigations have greatly improved our understanding of relativistic magnetic reconnection. Although within the incompressibility assumption, Lyutikov & Uzdensky (2003) first found that in the Sweet–Parker reconnection three different regimes can be produced, which depend on the ratio of the magnetization parameter $\sigma_{\rm m}$ to the Lundquist number S. Lyubarsky (2005), on the other hand, explicitly addressed the question about whether the reconnection rate can be significantly enhanced or not in the transition from Newtonian to relativistic magnetic reconnection. He found that, unless the reconnecting fields are not strictly antiparallel, the relativistic Petschek reconnection should not be considered as a mechanism for the direct conversion of the magnetic energy into the plasma energy, and the reconnection rate would be at most 0.1 the speed of light, contrary to what was originally suggested by Blackman & Field (1994). Moreover, Tolstykh et al. (2007) extended the Petschek reconnection model to incorporate relativistic effects of impulsive reconnection and, for current layers embedded into strong magnetic fields, they claimed that the plasma can be accelerated to high Lorentz factors.

Because our understanding of relativistic magnetic reconnection is still incomplete, in the last few years there has been a growing expectation towards numerical simulations as a promising tool for clarifying the rich underlying physics, particularly in the non-linear

★E-mail: zanotti@aei.mpg.de

[1] A similar mechanism has been proposed by Tanuma et al. (2003) to explain the X-ray emission in the Galactic halo.

regime. After the pioneering resistive relativistic simulations by Watanabe & Yokoyama (2006), who considered the Petschek-type reconnection in the relativistic regime with a resistive magneto-hydrodynamic (MHD) code, Zenitani, Hesse & Klimas (2009b) investigated the relativistic reconnection in an electron–positron plasma by a two-fluid MHD code and showed that the reconnection rate is higher and higher in magnetically dominated regimes. Zenitani, Hesse & Klimas (2009a), on the other hand, clarified the role of a guide magnetic field, which is essentially that of making the output energy flux Poynting dominated rather than enthalpy dominated. Very recently, Zenitani, Hesse & Klimas (2010) showed that, when the resistivity is current-dependent, plasmoids are repeatedly formed in the current sheet. In spite of these progresses, two major numerical limitations still prevent the application of numerical calculations to realistic physical and astrophysical scenarios in the relativistic regime. The first limitation manifests when treating plasmas with high magnetization parameters $\sigma_{\rm m}$, while the second limitation manifests when high Lundquist numbers S are encountered, being related to the stiffness of the equations in this regime. Physically, high Lundquist number plasmas are very interesting as they are supposed to become unstable and breakup into secondary magnetic islands. In the Newtonian framework, for example, Samtaney et al. (2009) showed that Sweet–Parker current sheets are unstable to super-Alfvénically fast formation of plasmoid chains for $S > S_{\rm c} \sim 10^4$, and it is not clear the extent to which this instability persists in a relativistic framework.

In this paper, by adopting the innovative numerical method presented in Dumbser & Zanotti (2009), we reconsider some of the scenarios discussed above within the relativistic MHD single-fluid approximation, focusing, in particular, on the dynamics of the plasma in a regime characterized by high Lundquist numbers, $S \sim 10^5$–10^8, and mild magnetization parameters $\sigma_{\rm m} \sim 1$–20.

We also investigate numerically, for the first time, the effect of an anisotropic Ohm's law, i.e. when the conductivity of the plasma is a tensor that depends on the orientation of the magnetic field.

The plan of the paper is the following. In Section 2, we report the relativistic resistive equations and the basic physical assumptions, while Section 3 is devoted to a succinct presentation of the numerical method and to the validation of the code in three space dimensions. Section 4 contains the results of our analysis, and Section 5 the conclusions. We have considered only flat space–times in pseudo-Cartesian coordinates, namely the metric $\eta_{\mu\nu} = {\rm diag}(-1, 1, 1, 1)$, where from now onwards we agree to use Greek letters $\mu, \nu, \lambda, \ldots$ (running from 0 to 3) for indices of 4D space–time tensors, while using Latin letters $i, j, k, \ldots$ (running from 1 to 3) for indices of 3D spatial tensors. We set the speed of light $c = 1$ and make use of the Lorentz–Heaviside notation for the electromagnetic quantities, such that all $\sqrt{4\pi}$ factors disappear. Finally, we use Einstein summation convention over repeated indices.

2 MATHEMATICAL FORMULATION

The total energy–momentum tensor of the plasma that we consider is made up by two contributions, $T^{\mu\nu} = T^{\mu\nu}_{\rm m} + T^{\mu\nu}_{\rm f}$. The first one is due to matter:

$$T^{\mu\nu}_{\rm m} = h\rho\, u^\mu u^\nu + p\eta^{\mu\nu}, \tag{1}$$

where u^μ is the four-velocity of the fluid, while h, ρ and p are the specific enthalpy, the rest-mass density and the pressure as measured in the comoving frame of the fluid. The second contribution comes from the electromagnetic field:

$$T^{\mu\nu}_{\rm f} = F^\mu{}_\lambda F^{\nu\lambda} - \tfrac{1}{4}(F^{\lambda\kappa}F_{\lambda\kappa})\eta^{\mu\nu}, \tag{2}$$

where $F^{\mu\nu}$, and its dual $F^{*\mu\nu}$, is the electromagnetic tensor given by

$$F^{\mu\nu} = n^\mu E^\nu - E^\mu n^\nu + \epsilon^{\mu\nu\lambda\kappa} B_\lambda n_\kappa \tag{3}$$

$$F^{*\mu\nu} = n^\mu B^\nu - B^\mu n^\nu - \epsilon^{\mu\nu\lambda\kappa} E_\lambda n_\kappa. \tag{4}$$

E^ν and B^ν are the electric and magnetic field as measured by the observer defined by the four-velocity vector n^μ, while $\epsilon^{\mu\nu\lambda\kappa} = [\mu\nu\lambda\kappa]$ is the completely antisymmetric space–time Levi-Civita tensor, with the convention that $\epsilon^{0123} = 1$. If we now set n^μ to define the inertial laboratory observer, namely $n^\mu = (1, 0, 0, 0)$, normalized such that $n^\mu n_\mu = -1$, then the four vectors of the electric and of the magnetic field are purely spatial, i.e. $E^0 = B^0 = 0$, $E^i = E_i$, $B^i = B_i$ in this frame. On the other hand, the fluid four-velocity u^μ and the standard three-velocity in the laboratory frame are related as $\boldsymbol{v} = v^i = u^i/\Gamma$, where $\Gamma = (1 - \boldsymbol{v}^2)^{-1/2}$ is the Lorentz factor of the fluid with respect to the laboratory frame.

In Cartesian coordinates, using the abbreviations $\partial_t = \frac{\partial}{\partial t}$ and $\partial_i = \frac{\partial}{\partial x_i}$, the full system of Euler and Maxwell equations are

$$\partial_t D + \partial_i (D v^i) = 0, \tag{5}$$

$$\partial_t S_j + \partial_i Z^i_j = 0, \tag{6}$$

$$\partial_t \tau + \partial_i S^i = 0, \tag{7}$$

$$\partial_t E^i - \epsilon^{ijk}\partial_j B_k + \partial_i \Psi = -J^i, \tag{8}$$

$$\partial_t B^i + \epsilon^{ijk}\partial_j E_k + \partial_i \Phi = 0, \tag{9}$$

$$\partial_t \Psi + \partial_i E^i = \rho_{\rm c} - \kappa\Psi, \tag{10}$$

$$\partial_t \Phi + \partial_i B^i = -\kappa\Phi, \tag{11}$$

$$\partial_t \rho_{\rm c} + \partial_i J^i = 0, \tag{12}$$

where the conservative variables of the fluid are

$$D = \rho\Gamma, \tag{13}$$

$$S^i = \omega\Gamma^2 v^i + \epsilon^{ijk} E_j B_k, \tag{14}$$

$$\tau = \omega\Gamma^2 - p + \tfrac{1}{2}(E^2 + B^2), \tag{15}$$

expressing, respectively, the relativistic mass density, the momentum density and the total energy density. The spatial tensor Z^i_j in (6), representing the momentum flux density, is

$$Z^i_j = \omega\Gamma^2 v^i v_j - E^i E_j - B^i B_j + \left[p + \tfrac{1}{2}\left(E^2 + B^2\right)\right]\delta^i_j, \tag{16}$$

where $\omega = h\rho$ is the enthalpy of the fluid, while δ^i_j is the Kronecker delta. An equation of state is needed to close the system, and we have chosen that of an ideal gas, namely

$$p = (\gamma - 1)\rho\epsilon = \gamma_1(\omega - \rho), \tag{17}$$

where γ is the adiabatic index, $\gamma_1 = (\gamma - 1)/\gamma$ and ϵ is the specific internal energy.

While writing equations (10) and (11), we have adopted the so-called *divergence-cleaning approach* presented in Dedner et al. (2002), which amounts to introducing two additional scalar fields Ψ and Φ that propagate away the deviations of the divergences of the electric and the magnetic fields from the values prescribed by Maxwell's equations. Additional details about this approach can be found in Komissarov (2007) and Palenzuela et al. (2009).

In its most general form, the relativistic formulation of Ohm's law is a non-linear propagation equation (Kandus & Tsagas 2008), which makes it manifest the connection between the Ohm's law and the equations of motion. However, in order to keep the equations numerically tractable and because of the poor knowledge of the conductivity in realistic conditions, simpler forms of the Ohm's law are usually considered, in which the currents are algebraically related to the electromagnetic field. Following Bekenstein & Oron (1978), we allow for an anisotropic Ohm's law, and therefore we write the four-current vector as

$$I^\mu = q_0 u^\mu + \sigma^{\mu\nu} e_\nu, \tag{18}$$

where q_0 is the charge density in the comoving frame of the plasma, $\sigma^{\mu\nu}$ is the conductivity tensor and e_ν is the electric field in the comoving frame. Within the collision-time approximation, the most general form of the conductivity tensor is given by

$$\sigma^{\mu\nu} = \sigma \left(g^{\mu\nu} + \xi^2 b^\mu b^\nu + \xi \epsilon^{\mu\nu\lambda\kappa} u_\lambda b_\kappa \right), \tag{19}$$

where u^μ is the four-velocity of the plasma and b^μ is the magnetic field in the comoving frame. The parameter ξ is related to the microphysics of the plasma (Bekenstein & Oron 1978) via $\xi = e\tau/m_\mathrm{e}$, where e and m_e are electron's charge and mass, while τ is the collision time. As a first application to the case of an anisotropic Ohm's law, in this paper we consider the case $\sigma^{\mu\nu} = \sigma(g^{\mu\nu} + \xi^2 b^\mu b^\nu)$, namely we drop the third term in (19). We note, therefore, that anisotropic effects in the Ohm's law are more and more important as the intensity of the magnetic field is increased. The four-current vector can also be decomposed in components parallel and perpendicular to the observer as $I^\mu = \rho_\mathrm{c} n^\mu + J^\mu$, where ρ_c is the charge density in the laboratory frame. Hence, it is easy to derive from (18) (see Appendix A for the calculations) the following expression for the spatial current vector to be used in equation (8), namely

$$\begin{aligned} \boldsymbol{J} &= \rho_\mathrm{c}\boldsymbol{v} + \Gamma\sigma\left[\boldsymbol{E} + \boldsymbol{v}\times\boldsymbol{B} - (\boldsymbol{E}\cdot\boldsymbol{v})\,\boldsymbol{v}\right] \\ &\quad + \Gamma\sigma\xi^2\,(\boldsymbol{E}\cdot\boldsymbol{B})\left[\boldsymbol{B} - \boldsymbol{v}\times\boldsymbol{E} - (\boldsymbol{B}\cdot\boldsymbol{v})\,\boldsymbol{v}\right]. \end{aligned} \tag{20}$$

Two relevant comments are worth doing about the Ohm's law (20). The first and most obvious one is that the isotropic regime is recovered when $\xi = 0$, in which case equation (20) reduces to the usual expression (Komissarov 2007). The second comment is that, in the comoving frame, the Ohm's law (20) becomes

$$\boldsymbol{J} = \sigma\boldsymbol{E} + \sigma\xi^2(\boldsymbol{E}\cdot\boldsymbol{B})\boldsymbol{B}, \tag{21}$$

which clarifies how the current term proportional to ξ^2 is present only for configurations for which $\boldsymbol{E}\cdot\boldsymbol{B} \neq 0$, and it is responsible for an extra current term in the direction parallel to the magnetic field.

3 NUMERICAL METHOD

3.1 Brief description

A well-known and challenging feature of the system of equations (5)–(12) is that it has source terms in the three equations (8) for the evolution of the electric field that become stiff in the limit of high conductivity. This pathology has been handled in the recent past by resorting to Strang-splitting techniques (Komissarov 2007) or to implicit–explicit Runge–Kutta methods (Palenzuela et al. 2009). In the present paper, on the other hand, we apply the strategy outlined by Dumbser & Zanotti (2009), who used the so-called high-order $P_N P_M$ methods, which are a unification of high-order finite volume and discontinuous Galerkin (DG) finite element schemes in a more general framework, and combining results from Dumbser, Enaux & Toro (2008b) and Dumbser et al. (2008a). It is worth stressing that, because of the high accuracy they allow us to achieve, Galerkin methods have been recently considered as a valuable approach even in fully relativistic calculations. Promising results have been obtained by Zumbusch (2009) and Radice & Rezzolla (2011).

In our specific implementation, the numerical solution of the vector of conserved quantities is represented at the beginning of each time-step by polynomials of degree N. However, the time evolution of these data and the computation of the corresponding numerical fluxes are performed with a different set of piecewise polynomials of degree $M \geq N$, which are reconstructed starting from the underlying N degree polynomials. The part of the algorithm performing the time evolution of the reconstructed polynomials uses a local space–time DG finite element scheme which provides a *local predictor* for constructing the solution of the partial differential equations *in the small*, as it was called by Harten et al. (1987). Our local space–time DG predictor allows us to discretize the stiff source terms arising in the resistive relativistic MHD equations naturally and without using any splitting techniques. The local space–time predictors are obtained after solving, for each individual cell element, a system of non-linear equations, which are therefore not globally coupled as in the global and fully implicit space–time Galerkin approach introduced by van der Vegt & van der Ven (2002) and Klaij, der Vegt & der Ven (2006). Once computed, the local space–time predictors are then inserted into a *global corrector*, which is fully explicit and provides the coupling between neighbouring cells. The resulting Galerkin scheme can allow for an arbitrary (at least in principle) order of convergence, through a one-step and quadrature free time update (no need for Runge–Kutta time-stepping) formula. Within this new approach, traditional finite volume schemes with $N = 0$ and usual DG methods with $N = M$ are included as special cases, while the new class of methods with $N \neq 0$, $M > N$ is in general computationally more efficient. In most of the numerical simulations reported in this paper, we have adopted the schemes P_0P_2, P_1P_2 and P_1P_3.

3.2 Validation of the code in three dimensions

In Dumbser & Zanotti (2009), we presented a wide class of numerical tests in both one and two spatial dimensions, showing the ability of the scheme in dealing with the stiff terms inherent in the resistive relativistic equations, while retaining its high-order properties. Here we complete the full validation of the code by considering the numerical evolution of a self-similar current sheet in three spatial dimensions. This configuration, first proposed by Komissarov (2007), has the following exact analytical solution for the y-component of the magnetic field:

$$B_y(x,t) = B_0\,\mathrm{erf}\left(\frac{1}{2}\sqrt{\frac{\sigma}{t}}x\right), \tag{22}$$

where erf is the error function. The initial time for this test case is chosen to be $t = 1$ and the initial condition at $t = 1$ is given by $\rho = 1$, $p = 50$, $\boldsymbol{E} = \boldsymbol{v} = 0$ and $\boldsymbol{B} = (0, B_y(x,1), 0)^\mathrm{T}$. We choose $\gamma = 4/3$ and $B_0 = 1$. The conductivity is set to $\sigma = 100$, which means a moderate resistivity. We have solved the problem with the fourth-order P_1P_3 scheme on a very coarse unstructured mesh composed by 3209 tetrahedrons. The grid extension is given by $[-1.5, 1.5] \times [-0.5, 0.5] \times [-0.25, 0.25]$ and it is shown in Fig. 1 with a colour rendering of the component B_y of the magnetic field. Fig. 2, on the other hand, shows the perfect matching of the numerical solution against the analytic one at time $t = 10$ and computed along a representative 1D cut of the numerical domain.

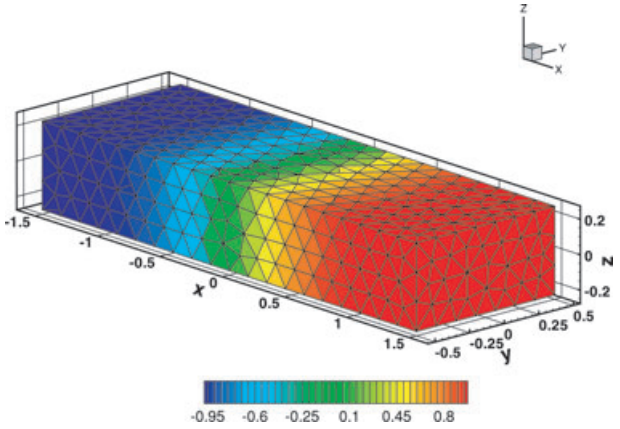

Figure 1. Numerical grid of the 3D simulation in the current sheet test. The B^y component of the magnetic field is reported.

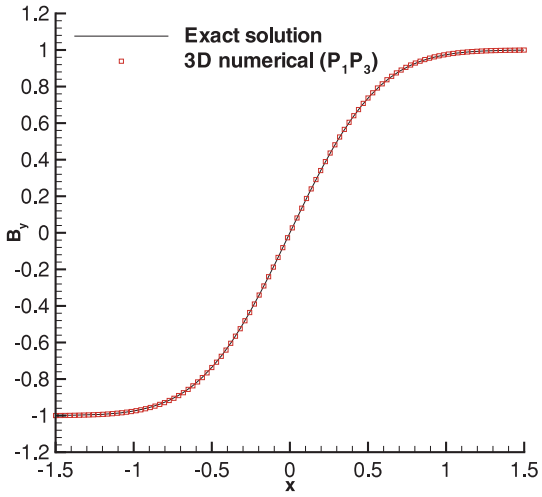

Figure 2. Comparison of the numerical solution with the analytic one in the 3D current sheet test. The plot shows a 1D cut of the magnetic field B^y at time $t = 10$.

We have also verified that the method provides the expected order of accuracy when the order of the polynomials in the $P_N P_M$ scheme is changed. This concludes the validation of the code in the full 3D case.

4 MAGNETIC RECONNECTION

4.1 Initial model and boundary conditions

The initial model that we have considered in our analysis of relativistic magnetic reconnection is built on the Harris model, as reported by Kirk & Skjæraasen (2003), and it reproduces a current sheet configuration in the x–y plane. Very similar configurations have been studied also by Watanabe & Yokoyama (2006) and Zenitani et al. (2009a,b). Gas pressure and density are given by $p = p_0 + \sigma_{\rm m}\rho_0[p_0 \cosh^2(2x)]^{-1}$ and $\rho = \rho_0 + \sigma_{\rm m}\rho_0[p_0 \cosh^2(2x)]^{-1}$, where p_0 and ρ_0 are the constant values outside the current sheet, whose thickness is $\delta = 1$. The magnetic field changes orientation across the current sheet according to $B_y = B_0 \tanh(2x)$, where the value of B_0 is given in terms of the magnetization parameter $\sigma_{\rm m} = B_0^2/(2\rho_0\Gamma_0^2)$. All over the grid there is a small background uniform resistivity $\eta_{\rm b}$, except for a circle of radius $r_\eta = 0.8$, defining a region of anomalous resistivity of amplitude $\eta_{i0} = 1.0$. As a result, the resistivity can be written as

$$\eta = \begin{cases} \eta_{\rm b} + \eta_{i0}\left[2(r/r_\eta)^3 - 3(r/r_\eta)^2 + 1\right] & \text{for} \quad r \le r_\eta, \\ \eta_{\rm b} & \text{for} \quad r > r_\eta, \end{cases} \tag{23}$$

where $r = \sqrt{x^2 + y^2}$. The velocity field is initially zero, hence $\Gamma_0 = 1$, while the electric field is given by $E_z = \eta(\partial B_y/\partial x)$. In most of our simulations, we have considered the case with $p_0 = 1$, $\rho_0 = 1$. The numerical grid consists of an unstructured mesh composed of triangles in 2D and tetrahedrons in 3D, which are clustered along the current sheet. The grid extension is given by $[-50, 50] \times [-150, 150]$ in 2D and by $[-50, 50] \times [-75, 75] \times [-12.5, 12.5]$ in 3D. Table 1 reports the basic parameters of the models studied in our simulations. The Lundquist number $S = v_{\rm A}L/\eta_{\rm b}$ is reported in the fourth column, where L is the length of the initial current sheet, while $v_{\rm A}^2 = B^2/(h\rho + B^2)$ is the relativistic Alfvén velocity (Komissarov 1997; Del Zanna et al. 2007). The names of the models have been chosen to facilitate recognizing their main parameters. For example, model 2D-m10-S2.68e5 is a 2D model with magnetization $\sigma_{\rm m} = 10$ and Lundquist number $S = 2.68 \times 10^5$ (corresponding to $\eta_{\rm b} = 10^{-5}$). We have used periodic boundary conditions at $y_{\rm min}$ and $y_{\rm max}$, while zeroth-order extrapolation is applied at $x_{\rm min}$ and $x_{\rm max}$.

Table 1. Main properties of the initial models. From left to right the columns report the name of the model, the magnetization parameter $\sigma_{\rm m}$, the Lundquist number S, the background resistivity $\eta_{\rm b}$, the value of the vertical magnetic field B_z, the number of cells used and the minimum cell size $L_{\rm min}$ (used for time-step calculation). All of the models have adiabatic index $\gamma = 4/3$, $p_0 = 1$, $\rho_0 = 1$ and $\eta_{i0} = 1.0$. A third-order P_0P_2 finite volume scheme has been adopted.

Model	$\sigma_{\rm m}$	S	$\eta_{\rm b}$	B_z/B_0	Cells	$L_{\rm min}$
2D-m1-S1.60e5	1.0	1.60×10^5	10^{-3}	0.0	844194	4.90×10^{-3}
2D-m5-S2.45e5	5.0	2.45×10^5	10^{-3}	0.0	844194	4.90×10^{-3}
2D-m10-S2.68e5	10.0	2.68×10^5	10^{-3}	0.0	844194	4.90×10^{-3}
2D-m15-S2.77e5	15.0	2.77×10^5	10^{-3}	0.0	844194	4.90×10^{-3}
2D-m20-S2.82e5	20.0	2.82×10^5	10^{-3}	0.0	844194	4.90×10^{-3}
2D-m10-S2.68e6	10.0	2.68×10^6	10^{-4}	0.0	844194	4.90×10^{-3}
2D-m10-S2.68e7	10.0	2.68×10^7	10^{-5}	0.0	844194	4.90×10^{-3}
2D-m10-S2.68e8	10.0	2.68×10^8	10^{-6}	0.0	844194	4.90×10^{-3}
3D-m1.25-Bz0	1.25	1.73×10^4	0.005	0.0	6105345	2.49×10^{-2}
3D-m1.25-Bz0.5	1.25	1.73×10^4	0.005	0.5	6105345	2.49×10^{-2}

4.2 Results

In a first series of simulations, we have considered the case of an isotropic Ohm's law, namely adopting equation (20) with $\xi = 0$, concentrating on the effects that an increasing magnetization produces on the system. Fig. 3 shows the rest-mass density and the magnetic field lines for the models 2D-m1-S1.68e5 with $\sigma_{\rm m} = 1.0$ (left-hand panel) and 2D-m20-S2.82e5 with $\sigma_{\rm m} = 20$ (right-hand panel). The two panels, which show snapshots of the two models at the same time $t = 90$, confirm the essential features of a Petschek-type relativistic reconnection, as also reported by other authors (Watanabe & Yokoyama 2006; Zenitani et al. 2009a,b). Namely, magnetic reconnection is triggered in the region of anomalous resistivity, producing the typical X-type topology of the magnetic field. As a result, magnetic energy is converted into both thermal and kinetic energy, and two plasmoids moving in opposite directions, and corresponding to the two high-density regions of the figure, are accelerated along

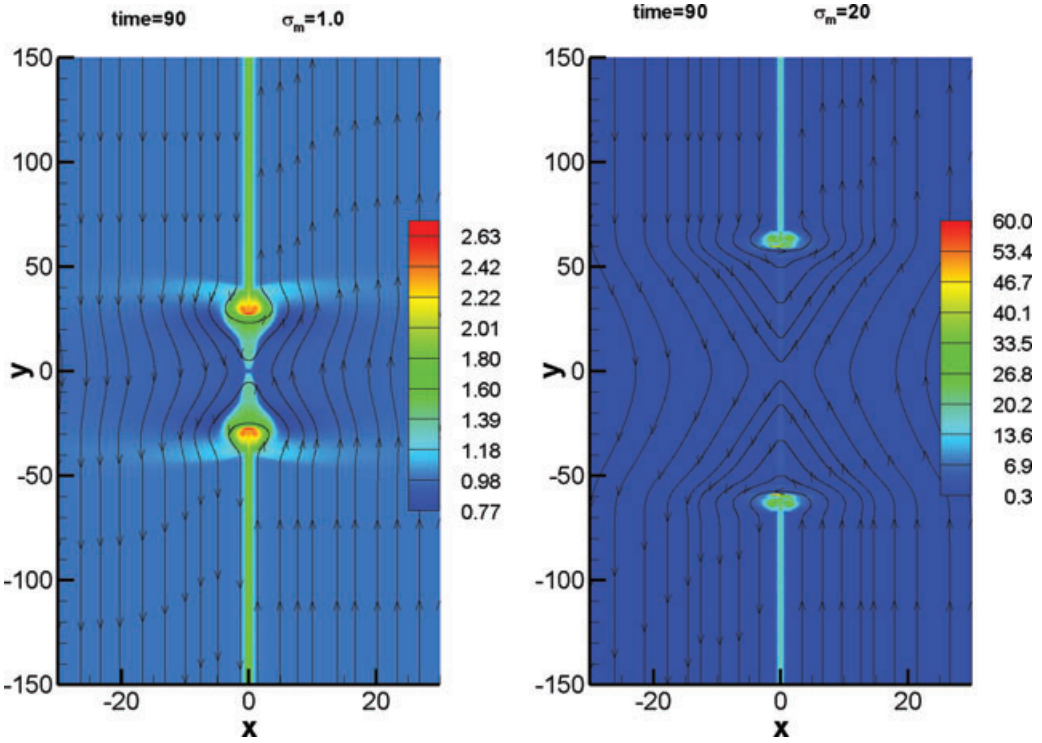

Figure 3. Colour map of the rest-mass density for two models with the same background electrical resistivity $\eta_b = 10^{-3}$ but different values of the magnetization: $\sigma_m = 1.0$ (left-hand panel) and $\sigma_m = 20$ (right-hand panel). Note that the aspect ratio of the figure is not 1.

the direction of the magnetic field. The magnetic tension, in fact, is responsible for the collimation of the flow. The plasmoid is highly compressed by plasma with much higher velocity and lower density (see the discussion about Fig. 5 below) and its rest-mass density increases with increasing magnetization. A complementary information to that of Fig. 3 is provided by Fig. 4. The top and the middle panels show, respectively, the time evolution of the magnetic energy (normalized to its initial value) and of the Lorentz factor of the plasmoid, which is also the maximum Lorentz factor monitored over the grid. The dissipated magnetic energy produces an increase of both the thermal and kinetic energy. The latter results in the acceleration of the plasmoid, which is more efficient for higher magnetizations. However, as the region around the anomalous resistivity becomes more and more rarefied, the conversion of magnetic energy into thermal energy becomes more efficient than the conversion into kinetic energy and the Lorentz factor reaches a saturation. The small wiggles visible in the Lorentz factor curves, particularly at high magnetizations, are due to impulsive reconnection episodes, taking place in very small and localized regions around the plasmoid. The bottom panel of Fig. 4, on the other hand, shows the maximum Lorentz factor reached as a function of the magnetization parameter. Our results show that, while at low magnetizations the Lorentz factor obeys a dependence of the kind $\Gamma \propto \sigma^{1/3}$, at higher magnetizations the dependence is close to the theoretical prediction given by $\Gamma \propto \sigma_m^{1/2}$ (Lyubarsky 2005; Zenitani et al. 2009b).

The reconnection rate, namely the speed at which the reconnection process takes place and that we have computed as[2] $r = E_z/B_0$, is also strongly dependent on the magnetization, as first noted by

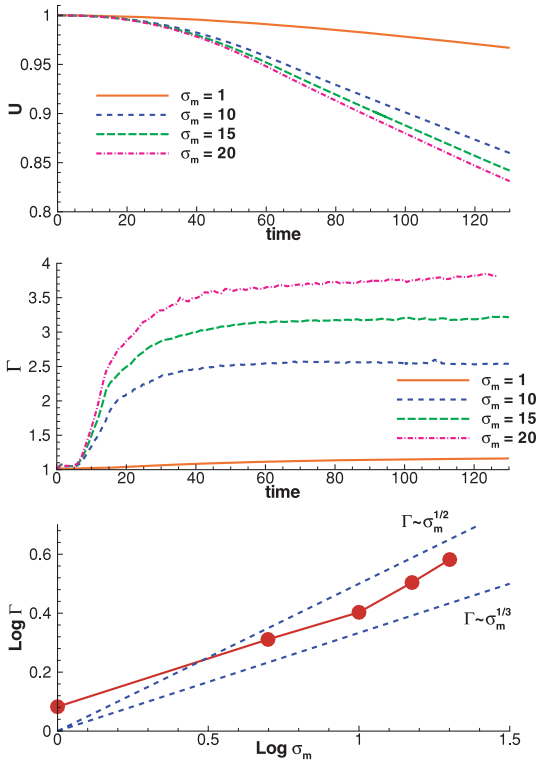

Figure 4. Time evolution of the magnetic energy (top panel) and the Lorentz factor (middle panel) for the first four models reported in Table 1 with increasing magnetizations σ_m. The bottom panel shows the dependence of the Lorentz factor on the magnetization in the plane $\log \sigma_m$–$\log \Gamma$.

[2] See Zenitani et al. (2009b) for alternative definitions of the reconnection rate.

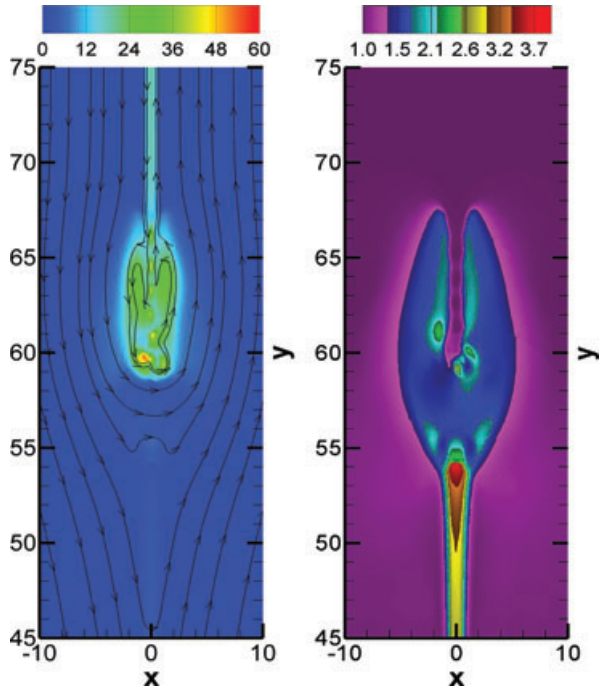

Figure 5. Colour map of the rest-mass density (left-hand panel) and the Lorentz factor (right-hand panel) for the model 2D-m20-S2.82e5 with $\sigma_{\rm m} = 20$ and $S = 2.82 \times 10^5$ at time $t = 90$.

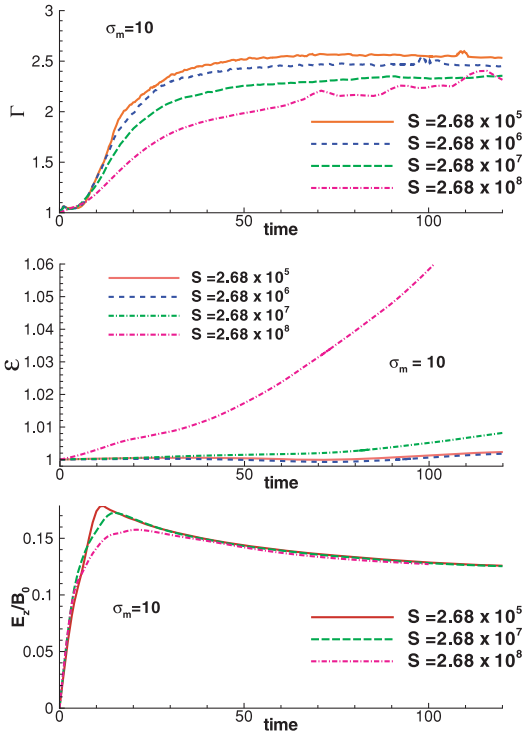

Figure 6. Time evolution of the Lorentz factor (top panel), thermal energy (middle panel) and reconnection rate E_z/B_0 (bottom panel) for models having the same magnetization $\sigma_{\rm m} = 10.0$ but different Lundquist numbers.

Watanabe & Yokoyama (2006). We have followed its temporal evolution and found that it reaches a maximum around $t \sim 20$–30, while decreasing asymptotically after that to reach a stationary value. The maximum reconnection rates are $r \sim 0.07$ and 0.2 for models with $\sigma_{\rm m} = 1.0$ and 20, respectively. It should be noted that the regions of maximum rest-mass density and maximum Lorentz factor do not match exactly. The mismatch is reported in Fig. 5, which provides a focus of the upper plasmoid that is visible in the right-hand panel of Fig. 3. The left- and right-hand panels of Fig. 5 show the rest-mass density and the Lorentz factor, respectively. As it is apparent from this figure, the plasma reaches its maximum velocity at the basis of the plasmoid in a very rarefied region. On the other hand, the portion of the plasmoid with maximum rest-mass density has very low Lorentz factor. As a result, a tiny bow shock is produced at the basis of the plasmoid, confirming similar findings by Zenitani et al. (2010), who performed a detailed analysis of the generation of slow shocks around the plasmoids.

In a second series of simulations, we have analysed the dependence of the reconnection process on the background Lundquist number S, while keeping the same peak values of the anomalous resistivity $\eta_{i0} = 1.0$ and the magnetization parameter $\sigma_{\rm m} = 10$. It is worth recalling that high values of S, corresponding to higher background conductivities, represent a challenge for the numerical scheme, as the stiffness of the resistive MHD equations becomes more severe. However, a higher resistivity jump between the background and the anomalous resistivity reproduces physical conditions where the plasma conductivity changes sharply over small distance scales, as expected in realistic conditions. The top panel of Fig. 6 shows that, when increasing the Lundquist number from $S = 2.68 \times 10^5$ to 2.68×10^8, the asymptotic Lorentz factor reached by the plasmoid is smaller. The explanation of this effect is once again to be found in the efficiency of magnetic energy conversion. When there is a higher conductivity jump between the central hotspot and the background, in fact, the fraction of magnetic energy that converts into thermal energy increases. This is shown in the middle panel of Fig. 6, which reports the time evolution of the specific internal energy of the plasma, which is higher for higher Lundquist numbers. The bottom panel of Fig. 6, on the other hand, shows the evolution of the reconnection rate $r = E_z/B_0$, whose peak is a mildly decreasing function of the Lundquist number. As it is evident from the top panel of Fig. 6, the Lorentz factor for the model with $S = 2.68 \times 10^8$ manifests an irregular evolution after $t = 70$, which is the signature of the development of a magnetic instability.

This effect is reported in Fig. 7, showing the rest-mass density in two models having different Lundquist numbers. No sign of instability is visible in simulations with Lundquist numbers as large as $S \sim 10^7$ (left-hand panel), while a chain of magnetic islands is produced for $S > S_{\rm c} \sim 10^8$ (right-hand panel). This instability, which resembles a tearing instability, was investigated through a linear analysis by Loureiro, Schekochihin & Cowley (2007), and subsequently confirmed via numerical simulations in the Newtonian framework by Samtaney et al. (2009). Our results, combined with those by Samtaney et al. (2009), indicate that, in the transition to the relativistic regime, the critical Lundquist number increases from $S_{\rm c} \gtrsim 10^4$ to 10^8. Such a conclusion may have deep implications for high Lundquist number reconnection in realistic astrophysical conditions, and it will deserve further investigations.

Finally, in a third series of simulations, we have considered the effects of the full anisotropic Ohm's law given by equation (20) with $\xi \neq 0$. In this case, a component of the magnetic field perpendicular to the x–y plane must be introduced, otherwise the term $\boldsymbol{E} \cdot \boldsymbol{B}$ in (20) remains zero. Hence, we have investigated anisotropic effects in three spatial dimensions and in configurations with $B_z \neq 0$, the so-called 'guide field' configurations (Lyubarsky 2005), for which we have chosen the value $B_z = 0.5B_0$. As a representative example, Fig. 8 shows the magnetic field B^2 on the slices

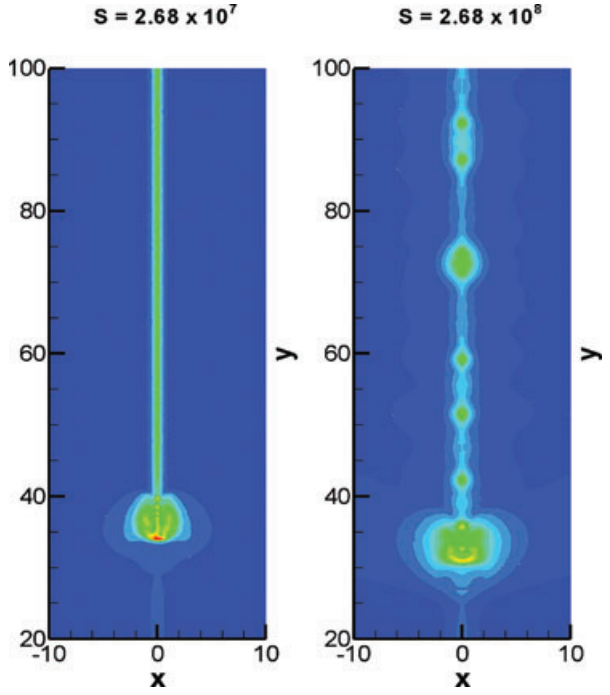

Figure 7. Generation of plasmoid chains in very high Lundquist numbers configurations. Left- and right-hand panels report, respectively, the colour map of the rest-mass density at time $t = 60$ for two models having $S = 2.68 \times 10^7$ and 2.68×10^8.

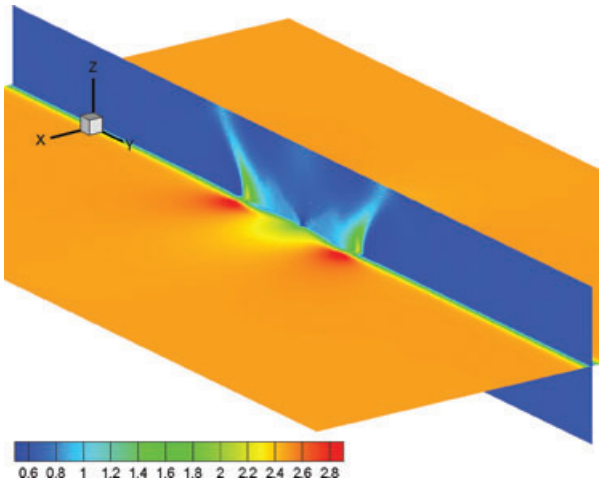

Figure 8. Magnetic field B^2 on the slices $x = 0$ and $z = 0$ for the model 3D-m1.25-Bz0.5 at time $t = 90$.

$x = 0$ and $z = 0$ for the model 3D-m1.25-Bz0.5 at time $t = 90$. The diffusion of the magnetic field is clearly visible in the region around the anomalous resistivity. It has to be remarked that, within our single-fluid approximation, inertial resistivity effects like those encountered by Zenitani et al. (2009a) cannot be captured and are not discussed here. Simulations with the guide field configuration in combination with the anisotropic Ohm's law turned out to be very challenging for the numerical scheme. In particular, strong magnetizations could not be reached and the results that we show here are limited to the case $\sigma_{\rm m} \sim 1$. When discussing the effects introduced by an anisotropic Ohm's law, we first need to distinguish them from those produced by the guide field. By using a two-fluid approach, Zenitani et al. (2009a) concluded that the guide field modifies the

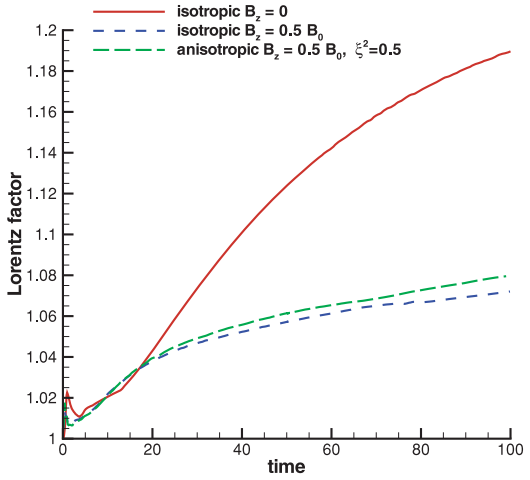

Figure 9. Combined effects of the guide field and anisotropic Ohm's law on the time evolution of the Lorentz factor. All of the models shown have $\sigma_{\rm m} = 1.25$. See text for explanation.

composition of the output energy flux, which, as the guide field increases, changes from being enthalpy dominated to being Poynting dominated. Even within a single-fluid approach, we confirm here a similar finding. This is shown in Fig. 9, where we compare the behaviour of three different configurations, each with an effective $\sigma_{\rm m} = 1.25$. The solid red and the dashed blue lines, in fact, refer, respectively, to a 3D simulation without the guide magnetic field and to a 3D simulation with the guide magnetic field, but with an otherwise isotropic Ohm's law. In the case of a non-zero guide field, the Lorentz factor is substantially smaller, while the decay of the magnetic energy, not reported here, is correspondingly slower. This is consistent with what was reported by Zenitani et al. (2009a), who found that the introduction of the guide field has the net effect of diminishing the bulk kinetic energy . Having clarified this, we have increased the parameter ξ to establish the extent to which results are affected by anisotropic Ohm's law (green long-dashed line). The present implementation of the numerical scheme does not allow us to treat the anisotropic parameter ξ as a true free parameter, and we have therefore concentrated on a mildly anisotropic regime. When ξ^2 is increased from 0 (isotropic case) to 0.5, the Lorentz factor indeed grows, but by 1 per cent only after $t = 100$. Intuitively, this effect can be explained in terms of the increased Lorentz force on the plasma, because of the extra current term on the right-hand hand side of (21). More work is needed to analyse the anisotropic regime under more realistic conditions.

5 CONCLUSIONS

We have investigated the dynamics of high Lundquist number relativistic magnetic reconnection, by performing 2D and 3D MHD simulations of a Petschek-type configuration. By resorting to high-order DG methods as proposed by Dumbser & Zanotti (2009), we have found that Lorentz factors up to ∼4 can be obtained for plasma parameters $\sigma_{\rm m}$ up to 20 in systems with Lundquist number $S \sim 10^5$. However, such values of the Lorentz factor decrease when S is increased as a result of a reduced background resistivity. When S is larger than a critical value $S_{\rm c} \sim 10^8$, the Sweet–Parker layer becomes unstable, generating a chain of secondary magnetic islands. This effect deserves additional theoretical investigations, in view of the fact that a similar instability has already been reported in the

Newtonian framework (Samtaney et al. 2009), but at much lower critical Lundquist numbers, i.e. for $S > S_c \sim 10^4$.

We have also shown that, when an anisotropic Ohm's law is adopted, both the reconnection rate and the Lorentz factor of the accelerated plasmoid are slightly increased. Although this increase is small and within a few per cent with respect to the isotropic Ohm's law, strongly anisotropic regimes remain challenging even for our advanced numerical scheme. We plan to improve on these limitations in our future applications of relativistic magnetic reconnection to the curved space–time around a neutron star, where an anisotropic Ohm's law can play a substantial role.

Finally, it is worth mentioning that pure MHD reconnection occurs in collisional plasmas, while the transition to collisionless reconnection is likely to enhance the reconnection rate (Uzdensky 2007; Uzdensky, Loureiro & Schekochihin 2010) and, presumably, also the acceleration properties. This possibility, which is related to some recent results of plasma physics (Bessho & Bhattacharjee 2007; Hesse et al. 2009), has been explored by Goodman & Uzdensky (2008) in accretion disc coronae and by McKinney & Uzdensky (2010) to trigger dissipation in gamma-ray burst jets. The numerical exploration of collisionless reconnection has received less attention[3] and it will represent another direction of our future analysis.

ACKNOWLEDGMENTS

OZ is grateful to Luciano Rezzolla and Serguei Komissarov for very useful discussions. Numerical simulations were performed on the National Supercomputer HLRB-II based on SGI's Altix 4700 platform and installed at Leibniz-Rechenzentrum. Partial support comes from the DFG grant SFB/Transregio 7, by 'CompStar', a Research Networking Programme of the European Science Foundation.

REFERENCES

Barkov M. V., Komissarov S. S., 2010, MNRAS, 401, 1644
Bekenstein J. D., Oron E., 1978, Phys. Rev. D, 18, 1809
Bessho N., Bhattacharjee A., 2007, Phys. Plasmas, 14, 056503
Blackman E. G., Field G. B., 1994, Phys. Rev. Lett., 72, 494
Dedner A., Kemm F., Kröner D., Munz C.-D., Schnitzer T., Wesenberg M., 2002, J. Comput. Phys., 175, 645
Del Zanna L., Zanotti O., Bucciantini N., Londrillo P., 2007, A&A, 473, 11
di Matteo T., 1998, MNRAS, 299, L15
Drenkhahn G., Spruit H. C., 2002, A&A, 391, 1141
Dumbser M., Zanotti O., 2009, J. Comput. Phys., 228, 6991
Dumbser M., Balsara D. S., Toro E. F., Munz C.-D., 2008a, J. Comput. Phys., 227, 8209
Dumbser M., Enaux C., Toro E. F., 2008b, J. Comput. Phys., 227, 3971
Goodman J., Uzdensky D., 2008, ApJ, 688, 555
Gruzinov A., 2005, Phys. Rev. Lett., 94, 021101
Harten A., Engquist B., Osher S., Chakravarthy S., 1987, J. Comput. Phys., 71, 231
Hesse M., Zenitani S., Kuznetsova M., Klimas A., 2009, Phys. Plasmas, 16, 102106
Jaroschek C. H., Lesch H., Treumann R. A., 2004, ApJ, 605, L9
Kandus A., Tsagas C. G., 2008, MNRAS, 385, 883
Kirk J. G., Skjæraasen O., 2003, ApJ, 591, 366
Klaij C., der Vegt J. V., der Ven H. V., 2006, J. Comput. Phys., 217, 589
Komissarov S. S., 1997, Phys. Lett. A, 232, 435
Komissarov S. S., 2007, MNRAS, 382, 995
Lazarian A., Kowal G., Vishniac E., de Gouveia dal Pino E., 2011, Planet. Space Sci., 59, 537
Loureiro N. F., Schekochihin A. A., Cowley S. C., 2007, Phys. Plasmas, 14, 100703
Lyubarsky Y. E., 2005, MNRAS, 358, 113
Lyutikov M., 2003, MNRAS, 346, 540
Lyutikov M., 2006, MNRAS, 367, 1594
Lyutikov M., Uzdensky D., 2003, ApJ, 589, 893
McKinney J. C., Uzdensky D. A., 2010, preprint (arXiv:1011.1904)
Nalewajko K., Giannios D., Begelman M. C., Uzdensky D. A., Sikora M., 2011, MNRAS, 413, 333
Palenzuela C., Lehner L., Reula O., Rezzolla L., 2009, MNRAS, 394, 1727
Pétri J., Lyubarsky Y., 2007, A&A, 473, 683
Radice D., Rezzolla L., 2011, Phys. Rev. D, 84, 024010
Rezzolla L., Giacomazzo B., Baiotti L., Granot J., Kouveliotou C., Aloy M. A., 2011, ApJ, 732, L6
Samtaney R., Loureiro N. F., Uzdensky D. A., Schekochihin A. A., Cowley S. C., 2009, Phys. Rev. Lett., 103, 105004
Schopper R., Lesch H., Birk G. T., 1998, A&A, 335, 26
Tanuma S., Yokoyama T., Kudoh T., Shibata K., 2003, ApJ, 582, 215
Tolstykh Y. V., Semenov V. S., Biernat H. K., Heyn M. F., Penz T., 2007, Advances Space Res., 40, 1538
Uzdensky D. A., 2003, ApJ, 598, 446
Uzdensky D. A., 2007, ApJ, 671, 2139
Uzdensky D. A., Loureiro N. F., Schekochihin A. A., 2010, Phys. Rev. Lett., 105, 235002
van der Vegt J. J. W., van der Ven H., 2002, J. Comput. Phys., 182, 546
Watanabe N., Yokoyama T., 2006, ApJ, 647, L123
Zenitani S., Hesse M., Klimas A., 2009a, ApJ, 705, 907
Zenitani S., Hesse M., Klimas A., 2009b, ApJ, 696, 1385
Zenitani S., Hesse M., Klimas A., 2010, ApJ, 716, L214
Zumbusch G., 2009, Classical Quantum Gravity, 26, 175011

APPENDIX A: DERIVATION OF EQUATION (21)

We first write the fluid four-velocity, the magnetic field in the comoving frame and the electric field in the comoving frame as

$$u^\mu = \Gamma(v^\mu + n^\mu) \tag{A1}$$

$$e^\mu = F^{\mu\nu}u_\nu = \Gamma[n^\mu(\boldsymbol{v}\cdot\boldsymbol{E}) + E^\mu + (\boldsymbol{v}\times\boldsymbol{B})^\mu] \tag{A2}$$

$$b^\mu = F^{*\mu\nu}u_\nu = \Gamma[n^\mu(\boldsymbol{v}\cdot\boldsymbol{B}) + B^\mu - (\boldsymbol{v}\times\boldsymbol{E})^\mu], \tag{A3}$$

where we have used the definitions (3) and (4) for the electromagnetic tensor and where we have used the property $\epsilon^{\mu\nu\lambda} = \epsilon^{\mu\nu\lambda\kappa}n_\kappa$. We then refer to the relation

$$\sigma^{\mu\nu} = \sigma(g^{\mu\nu} + \xi^2 b^\mu b^\nu) \tag{A4}$$

and after noticing that $b^\mu e_\mu = \boldsymbol{E}\cdot\boldsymbol{B}$ (it is a relativistic invariant), we rewrite (18) as

$$I^\mu = q_0\Gamma(v^\mu + n^\mu) + \sigma\Gamma[(\boldsymbol{v}\cdot\boldsymbol{E})n^\mu + E^\mu + (\boldsymbol{v}\times\boldsymbol{B})^\mu] + \sigma\xi^2(\boldsymbol{v}\cdot\boldsymbol{E})\Gamma[(\boldsymbol{v}\cdot\boldsymbol{B})n^\mu + B^\mu - (\boldsymbol{v}\times\boldsymbol{E})^\mu]. \tag{A5}$$

At this point, we compare (A5) with $I^\mu = \rho_c n^\mu + J^\mu$ to find

$$\rho_c = q_0\Gamma + \sigma\Gamma(\boldsymbol{v}\cdot\boldsymbol{E}) + \sigma\xi^2\Gamma(\boldsymbol{E}\cdot\boldsymbol{B})(\boldsymbol{v}\cdot\boldsymbol{B}) \tag{A6}$$

$$J^\mu = q_0\Gamma v^\mu + \sigma\Gamma E^\mu + \sigma\Gamma(\boldsymbol{v}\times\boldsymbol{B})^\mu + \sigma\xi^2(\boldsymbol{E}\cdot\boldsymbol{B})\Gamma[B^\mu - (\boldsymbol{v}\times\boldsymbol{E})^\mu]. \tag{A7}$$

A last replacement of q_0 from (A6) into (A7) allows us to derive (20) of the main text.

This paper has been typeset from a TEX/LATEX file prepared by the author.

[3] Also note that Lazarian et al. (2010), after solving numerically a reduced set of equations, showed that reconnection in a turbulent fluid occurs at a rate comparable to the rms velocity of the turbulence, irrespective of the degree of collisionality.